energy&fuels

pubs.acs.org/EF Article

Nanostructural Disorder and Reactivity Comparison of Flame Soot and Engine Soot Using Diesel and Jatropha Biodiesel/Diesel Blend as Fuels

Pranay P. Morajkar, Moataz K. Abdrabou, Akshay V. Salkar, Abhijeet Raj,* Mirella Elkadi, and Dalaver H. Anjum

Cite This: *Energy Fuels* 2020, 34, 12960−12971 Read Online

ACCESS | Metrics & More | Article Recommendations | Supporting Information

ABSTRACT: Soot is a major anthropogenic air pollutant that affects human health and contributes to global warming. To understand its formation pathways and reduce emission, several flame and engine studies exist in the literature, though the fundamental differences in the characteristics of engine and flame soots are not well understood. This study presents a detailed comparative investigation of soot nanostructural properties and their relationship with the oxidative reactivity of soots from an engine and a diffusion flame using diesel and 20% Jatropha biodiesel/diesel blend fuels. X-ray diffraction, Raman spectroscopy, high-resolution transmission electron microscopy, electron energy loss spectroscopy, and thermogravimetric analyses confirm that engine soot has greater primary particle diameter, higher concentration of loosely held aliphatics, greater degree of graphitized nanocrystallites with lower interplanar separation, longer fringe lengths, lower tortuosity, and greater resistance for oxidation than the flame soot, though the differences in several properties were minor. The effects of biodiesel addition to diesel on soot properties and sooting tendency were predicted very well with both flame and engine setup. Moreover, the enhanced soot oxidation in the combustor catalyzed by fuel-bound oxygen in biodiesel further reduces the nanostructural and reactivity differences between engine and flame soots. Though engine soot properties have more relevance to anthropogenic particulate matter, flame setups appear to be suitable for screening and studying the effect of fuel additives on the sooting propensity and physicochemical properties of soot prior to their testing and utilization in engines.

1. INTRODUCTION

Air pollution and climate change are important environmental issues of the present decade. The degrading air quality due to anthropogenic emission of pollutants such as CO, NO_x, SO_x, and soot via the combustion of fossil fuels has become the major source of air pollution.[1,2] CO, NO_x, and SO_x mitigation is being addressed via engine design modifications and improvements in fuel quality and catalytic converters.[3] Curbing soot emission economically remains a challenge. Though diesel particulate filters (DPFs) have been very effective in capturing soot, their cost has limited their usage in developing countries. Soot, a carbonaceous material consisting of randomly oriented stacks of polycyclic aromatic hydrocarbons (PAHs), is formed due to the incomplete combustion of fuels via nucleation−condensation−growth processes.[4] Many of these PAHs are known carcinogens.[5] Recent findings suggest that soot influences regional climate and enhances melting of polar icecaps to contribute to global warming.[6] Therefore, several strict legislations and regulatory policies are being implemented across the world to optimize engine designs, DPF technologies, and advanced fuel designs as mitigation steps.[7]

The studies on physicochemical characteristics of soot help in understanding its formation mechanisms and reactivity and in finding methods to reduce its emission. The oxidative reactivity of soot is considered extremely important, as more reactive soot is easily oxidized in the engine and in DPF to lead to its faster regeneration at relatively lower temperature.[8] Therefore, a great deal of research focus has been devoted to elucidate the chemical composition, morphology, and nanostructural characteristics of soot particles.[9] The soot nanostructure and its disorder are greatly influenced by the combustion conditions and the type of fuel additive. Improved engine performance and soot suppression potential have been reported so far by blending diesel with oxygenated biofuels such as bio-alcohols,[10] biodiesels from Jatropha,[11] Karanja,[12] palm oil,[13] and camphor oil.[14] Interestingly, each biofuel, depending on the chemical structure and functional groups such as oxygen content, degree of unsaturation, existence of five-membered cyclic structure, number of aromatic rings, and C/H ratio, significantly influences the soot formation rate and its oxidative reactivity.[15] Along with the fuel properties, soot reactivity is also affected by the presence of chemical functionalities on soot structure found through infrared techniques such as diffuse reflectance infrared Fourier transform spectroscopy (DRIFTS), as reported in ref 16.

Received: June 22, 2020
Revised: September 20, 2020
Published: September 23, 2020

https://dx.doi.org/10.1021/acs.energyfuels.0c02063
Energy Fuels 2020, 34, 12960−12971

Several studies on the influence of engine operating parameters such as engine load, speed, fuel injection pressure, and fuel physical parameters such as density, viscosity, and molecular weight on soot emission potential of a fuel have been reported.[17] However, some disagreements also exist in the literature regarding the nanostructural characteristics of soot and its oxidative reactivity. For instance, Ruiz et al.[18] studied alcohol−diesel blends in a direct-injection diesel engine and observed that the fringe separation in soot decreases as the engine load increases, but they found no influence of engine load on crystallite parameters using bio-alcohols. On the contrary, X-ray diffractometer (XRD) analysis of soot collected from a twin-cylinder diesel engine by Braun et al.[19] led to the conclusion that soot parameters such as PAH stack size (L_a) and PAH stack height (L_c) increase as the engine load is increased. Raman spectroscopic analysis of soot in engines[20−22] suggests that, as the engine load increases, the nanostructural order in soot increases. The primary particle diameter of soot reduces when biodiesel is blended with diesel,[22] and also when engine load is increased as a result of high in-cylinder temperature that favors soot oxidation overgrowth. The effect of injection timing on soot crystallite parameters remains largely inconclusive.[23]

High-resolution transmission electron microscopy (HRTEM) analysis has been crucial in providing evidence of soot nanostructural disorder. For instance, Verma et al.[24] found that, by increasing the oxygen content in the butanol−diesel blends, soot fringe length and fringe separation increased, while the tortuosity decreased. On the contrary, in the study on waste cooking oil methyl ester−diesel blends by Man et al.,[25] it was observed that the reduction in soot emission in a DI engine is a result of greater oxidative reactivity due to shorter fringe length and greater tortuosity of diesel engine soot. Such contradictions in understanding soot nanostructural disorder and oxidative reactivity arises because the engine operating parameters such as engine speed, load, fuel injection system, exhaust gas recirculation, temperature, and pressure simultaneously influence the soot formation and oxidation mechanisms. This makes it complicated to derive a realistic and confirmative evidence that can specifically highlight the actual effect of the additive on the sooting tendency of a fuel and detect the influence of the additive's chemical structure on the soot's nanostructural disorder and reactivity. Therefore, flame setups are also used to study sooting tendencies of fuels with or without additives.[26−28]

While several fuel additives and their effects on soot nanostructure and oxidative reactivity have been independently studied by several research groups using either engines or flames, there is no systematic comparative analysis of the differences in the nanostructural characteristics of soot generated from a given fuel using an engine and a flame test together. Maricq[29] presented a study comparing flame and engine soots, although different fuels were tested in each method (ethylene and propane in flames and gasoline and diesel in engines). The results were compared in terms of black carbon content in flame and engine soots, but for flame soots, particle size distribution was also presented. It was found that flame soots matched the black carbon content of engine soots fairly well and that the flame soots could act as a surrogate for particulate matter from engines, although no comparisons on nanostructures in soots and their reactivity (physicochemical properties) were presented. The engine operating conditions are different from the flame tests in terms of operating conditions such as temperature, pressure, residence time, and fuel−air mixing ratios, which may affect the radical reactions, leading to soot formation, which, as a result, may affect soot's morphology, nanostructural characteristics, chemical composition, distribution of aromatic/aliphatic content, and reactivity. The comparison of soots from flames and engines could provide crucial information such as (a) if flame-generated soot characteristics are substantially different from engine soots, when same fuel is used in both setups, and (b) if the results of sooting tendencies of fuels and soot reactivity studies conducted using flames could be extrapolated to engine soot emissions and the efficiency of DPF regeneration.

The present study provides a systematic investigation on the nanostructural characteristics and the oxidative reactivity of soots generated from the combustion of diesel and 20% Jatropha biodiesel/80% diesel blend in both an engine and a diffusion flame. The analysis of nanostructural characteristics of soot such as fringe length, tortuosity, primary particle diameter, PAH stack size, and aliphatic/aromatic ratio and their influence on the oxidative reactivity of soots generated from an internal combustion engine and a standard smoke point flame setup are discussed. This study provides a rational estimate for evaluating fuel additives and their soot suppression potential based on the type of combustion method used.

2. EXPERIMENTAL DETAILS

2.1. Fuel Properties. The commercial diesel fuel (Grade No. 2-D S15, ASTM D975[30]) was obtained from a local fuel station from Abu Dhabi, UAE, and Jatropha biodiesel was purchased from SVM Agro Processor, India. The two fuels were completely miscible without any phase separation. The physical properties of both pure diesel and the Jatropha biodiesel blends were measured, and the results are displayed in Table 1. A Stabinger Viscometer (SVM 3000, Anton Paar) was used to measure the kinematic viscosity and the density of the fuel blends following the procedure as per the ASTM D7042 standard.[31] The calorific values of the tested fuels were found using the ASTM D240 standard technique. All tests were run using the same batch of fuels to have consistency in the results.

Table 1. Characteristics of Fuels and Flames

physical properties	diesel		20% Jatropha 80% diesel	
density (kg/m^3)	829		842.7	
dynamic viscosity (kg/m·s)	0.00289		0.00297	
kinematic viscosity (mm^2/s)@20 °C	3.49		3.52	
heating value, MJ/kg	43.4[a]		42.2[a]	
flash point, °C	94.4[a]		99.3[a]	
	Flame	Engine	Flame	Engine
fuel flow rate (mL/h)	3.47	800	2.56	625
soot production rate (mg/h)	4.2	2.05	3.3	1.08

[a]Calculated using correlations, as shown in the Supporting Information. The calculated values match well with the range of values reported in the literature.

2.2. Smoke Point Apparatus. Smoke point apparatus serves as a standard laboratory instrument to evaluate the sooting tendency of a fuel.[32] This procedure was noted to have certain advantages over the diesel engine setup. For instance, it is free from impurities generated from lubricating oil and wear and tear of the engine parts. Moreover, the flame conditions can be easily tuned to achieve highly sooting flames easily unlike the engines. The smoke point apparatus (RAP172) was utilized to produce diffusion flames at atmospheric pressure and perform experiments using the standard ASTM D1322-08 procedure.[30] A detailed representation of the smoke point setup is

https://dx.doi.org/10.1021/acs.energyfuels.0c02063
Energy Fuels 2020, 34, 12960−12971

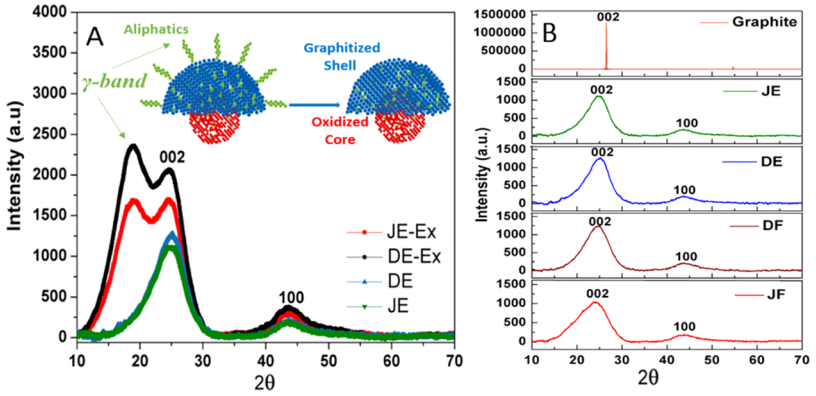

Figure 1. (A) XRD pattern of diesel and 20% Jatropha 80% diesel soot from engine before (DE-Ex, JE-Ex) and after (DE, JE) heat treatment in Ar at 300 °C with a schematic (inset) depicting elimination of aliphatic side chains upon heat treatment. (B) Overlay of XRD patterns of all engine- and flame-generated soot samples in comparison to graphite.

shown in Supporting Information Figure S1A. Briefly, in the smoke point apparatus, (i) the fuel is filled in a cylindrical fuel reservoir, in which a cotton wick is soaked and the tip is ignited to produce the flame, (ii) the flame is housed in a metallic body with a scale behind the flame, which is read through a glass door in front of the flame, and (iii) a long chimney at the upper end contains a perpendicularly mounted borosilicate microfiber filter assembly (from Sierra Instruments). The use of a suction pump allows trapping of soot particles on the filter.[33] With the aid of this lab-scale setup, the pure diesel fuel and the blend of Jatropha biodiesel and diesel were tested. The smoke point of diesel was 19 mm, while that of 20% Jatropha biodiesel/80% diesel was 25 mm. Soot particles were collected 2 mm above the respective smoke point values to be able to generate enough soot for characterization. Flame soot from pure diesel was labeled as DF, while that from 20% Jatropha biodiesel/80% diesel was labeled as JF. Above 20% biodiesel in the blend, it was difficult to keep the flame height constant in the smoke point apparatus for a long time, and it frequently suffered from flame extinction due to the reduced energy density of the blended fuel. This makes it difficult to obtain reliable experimental data. This has also been highlighted before.[34,35] Thus, we did not perform experiments at higher blending percentages.

2.3. Diesel Engine Setup. Fuel combustion and soot formation were also studied in a four-stroke, direct-injection diesel engine with a single cylinder that is fixed at a constant rotation speed. The layout of the diesel engine setup is shown in Figure S1B, and its detailed specifications are shown in Table S1 of the Supporting Information. With the aid of this fixed diesel engine setup, two sets of soot samples were collected by mounting the soot collection microfiber assembly perpendicular to the engine exhaust line assisted with a suction pump. Soot generated using pure diesel fuel was denoted as DE, while the soot from 20% Jatropha biodiesel/80% diesel blend was labeled as JE.

2.4. Material Characterization. The collected soot samples were heat-treated at a rate of 20 °C/min at 300 °C under Ar flow and were subsequently used for chemical and structural characterization. For high-resolution transmission electron microscopy (HRTEM) analysis, the soot samples were dispersed in ethanol under sonication for 5 min, and a drop of this mixture was added onto the Lacey carbon-coated Cu TEM grid. The TEM grid was then air-dried, and the HRTEM analysis was performed using a spherical aberration-corrected microscope of Titan 80-300ST model from Thermo Fisher Scientific that was equipped with an electron energy loss spectrometer (EELS) of GIF Quantum 963 model from Gatan, Inc. The microscope was operated at an accelerating voltage of 300 kV during the analysis of samples. First, the aberration-corrected imaging analysis[36] was applied to measure the size and shape of soot particles present in the samples. Several images containing low and high resolutions were recorded in this mode using the charge-coupled device (CCD) camera of US1000 model from Gatan, Inc. The fraction of graphitized carbon present in the samples was determined by figuring out the fraction of sp^2 hybridization in the sample from the acquired EELS spectra. The complete details of carrying out this exercise can be found in ref 37. The entire data acquisition and subsequent image analysis were performed in Gatan Microscopy Suite (GMS) of version 3.2.

A thermogravimetric analyzer (TGA, NETZSCH STA 409PC-LUXX) was utilized to measure soot oxidative reactivity in air under temperature-programmed conditions with heating rates of 1, 3, and 5 °C/min in the region of 300−800 °C.[33] The X-ray diffraction patterns of soots were recorded in the range of 10−90° using a PANalytical Empyrean X-ray diffractometer (XRD).[33] The soot structural parameters such as length of the PAHs (L_a), thickness or height of the stack (L_c), and spacing between graphene layers (d_{002}) were calculated. A Witech α 300 RAS instrument containing a 515 nm laser source and a dual-purpose 50× objective lens was used to record the Raman spectra, which were subsequently deconvoluted using Origin Pro software, and the ratio of disordered D band to graphitic G band was calculated.

3. RESULTS AND DISCUSSION

3.1. Effect of Jatropha Biodiesel//Diesel Blending on Soot Production. From Table 1, it is evident that the diesel fuel has a lower density and kinematic viscosity compared to the blended fuel. The higher density and viscosity of the blended fuel resulted in a relative decrease in its fuel flow rate compared to diesel in the flame setup by 26% and in the engine setup by 22%. Nevertheless, the above limitation is greatly compensated by the increased cetane number of the blend (≈58) compared to diesel (≈51), which results in improved combustion and reduced emission rates of CO, HC, and particulate matter, as reported by Datta et al.[38] The overall soot production rates with both the fuels in the engine setup were lower than those in the flames, which is expected since flames were being operated in the high-sooting zones (above the smoke point at high fuel flow rate to purposefully produce more soot), while the engine is designed for efficient fuel combustion to lead to less soot. With the addition of Jatropha biodiesel to diesel in the flame setup, the soot production rate reduced by 51%, while in the engine setup, it was reduced by 67%. The more significant effect, observed in the engine setup, is possibly a result of improved combustion of blended fuel with increased cetane number, as mentioned earlier. The soot generated from the engine and the flame setups were then subjected to a series of surface characterization tests, and the results of these tests are analyzed and discussed in detail in the subsequent sections.

3.2. X-ray Diffraction. The X-ray diffraction method serves as an effective tool for elucidating the bulk crystal

https://dx.doi.org/10.1021/acs.energyfuels.0c02063
Energy Fuels 2020, 34, 12960−12971

Table 2. Summary of Calculated Soot Nanocrystallite Parameters[a]

properties	sample			
	DE soot	DF soot	JE soot	JF soot
	XRD Results			
interlayer spacing, d_{002}	0.350 nm	0.354 nm	0.364 nm	0.375 nm
nanocrystallite height, L_c	1.349 nm	1.246 nm	1.030 nm	1.004 nm
nanocrystallite width, L_a	3.067 nm	2.989 nm	2.845 nm	2.786 nm
L_c/d_{002} (no. of layers, N)	3.80	3.52	2.83	2.68
	HRTEM Results			
mean fringe length	1.61 nm	1.77 nm	1.49 nm	1.3 nm
mean fringe tortuosity	1.74	1.95	2.10	2.25
primary particle diameter	36.7 nm	21.3 nm	18.7 nm	18.3 nm
	Raman Results			
I_{D1}/I_G ratio	1.01	1.27	1.30	1.36
lattice width, L_a	3.9 ± 0.5 nm	3.38 ± 0.5 nm	3.31 ± 0.5 nm	3.16 ± 0.5 nm

[a]DE: diesel soot from engine, DF: diesel soot from flame, JE: 20% Jatropha biodiesel/80% diesel blend soot from engine, and JF: 20% Jatropha biodiesel/80% diesel blend soot from flame.

structure disorder in soot samples. The background-corrected XRD pattern of soot samples (DF, JF, DE, and JE) are shown in Figure 1A,B. The XRD pattern of the "as-obtained" engine soot without heat treatment showed the typical broad peaks at 2θ values of around 25° and 44°, but an additional peak of high intensity, called as the γ-band, at around 19° was observed. The γ-band could be attributed to loosely held long-chain aliphatic structures (i.e., highly amorphous carbon resulting from unburned fuel or hydrocarbons adsorbed on soot surface, possibly during soot collection on the filters), as depicted in the schematic (inset) in Figure 1A. Some literature studies also attribute this γ-band to the amorphous carbon at the edges of contiguous crystallites or even to the subsequent bulking and exfoliation of carbon layers.[9,39] The concentration of such aliphatic molecules was significantly greater in diesel engine soot (DE) compared to biodiesel-blended diesel engine soot (JE), as evident from the high intensity of the (002) peak in DE. This is due to the reduction in unburned hydrocarbon concentration with the addition of Jatropha biodiesel to diesel, as observed in engine experiments in ref 38. Such a γ-band structure was missing from the XRD patterns of flame-generated soot samples DF and JF since the fuel flow rate in flames is significantly lower compared to that in engine (Table 1) that lead to lower amounts of unburned hydrocarbons per unit time emanating from flames to adsorb on soot. This is an interesting difference between the raw soots from the flame test and the engine. However, upon drying these soot samples at 300 °C in Ar gas atmosphere, the loosely held aliphatic compounds got separated from the engine soots, which allowed a systematic comparative analysis of the peak positions, crystal lattice parameters, and the structural disordered analysis of the soot samples derived from the two combustion devices (see Figure 1B and Table 2). The graphite sample (99%, 325 mesh particle size; Sigma-Aldrich) was used as a reference for comparison. The XRD pattern of graphite exhibited very high intensity peaks at 2θ values of 26.4 and 54.6° with an interlayer separation of 0.335 nm. The extensive broadening and the low intensity of the (002) and (100) peaks and a relative shift to lower 2θ values, as observed in all soot samples in comparison to graphite, are a clear indicator of the excessive crystal disorder in soot samples due to random orientations of the PAH nanocrystallites present in both engine and flame soots. The Bragg angles (θ_{002} and θ_{100}) and the full width at half-maximum (FWHM) were obtained via Gaussian fitting of the respective peaks using MATLAB software. The PAH interlayer spacing (d_{002}) and thickness of the PAH stack (L_c) were obtained from the above analysis of the peak at 25°, while the average longitudinal size (i.e., nanocrystallite width, L_a) of the PAH stack is calculated from the (100) peak at 44° using eqs EE1−EE3, respectively. In eqs EE2 and EE3, the values 0.9 and 1.84 represent experimental shape factors.[9,40] The obtained values are listed in Table 2.

$$d_{002} = \frac{\lambda}{2 \sin \theta_{002}} \quad \text{(E1)}$$

$$L_c = \frac{0.9\lambda}{B_{002} \cos \theta_{002}} \quad \text{(E2)}$$

$$L_a = \frac{1.84\lambda}{B_{100} \cos \theta_{100}} \quad \text{(E3)}$$

As evident from the table, all of the soot samples exhibited greater interlayer separation (d_{002}) than graphite. The interlayer spacing within the PAH stacks for engine soots was slightly lower than that for flame-derived diesel soots. A comparison between the DE and JE soots (and DF and JF soots) confirms that the addition of Jatropha biodiesel to diesel results in an increase in the interlayer separation within the PAH stacks (in agreement with the observations of Verma et al.[24]). This effect of biodiesel on diesel soot was captured in both flame and engine setups. The greater interlayer spacing is an indicator of lower binding energy within the PAH stacks (also arising from smaller PAHs in stacks), which could make soot more disordered in structure and more prone to oxidation by O_2 or radicals.[41] However, when JE and JF soots are compared, the interlayer separation in flame-derived soot is marginally greater in the engine-derived soot, suggesting a possible graphitization effect.[42] This graphitization effect is expected to be more dominant under the engine conditions (higher pressure and temperature[29]) compared to a flame setup. As shown in Table 2, the crystallite parameters, L_c, L_a, and the number of layers in a PAH stack in engine soots from a given fuel were only slightly higher than their values in flame soots. However, these parameters for diesel soots (DE and DF) were notably greater than those for Jatropha biodiesel-blended diesel soots (JE and JF), and both flame and engine setups could capture this trend. For example, the biodiesel

https://dx.doi.org/10.1021/acs.energyfuels.0c02063
Energy Fuels 2020, 34, 12960−12971

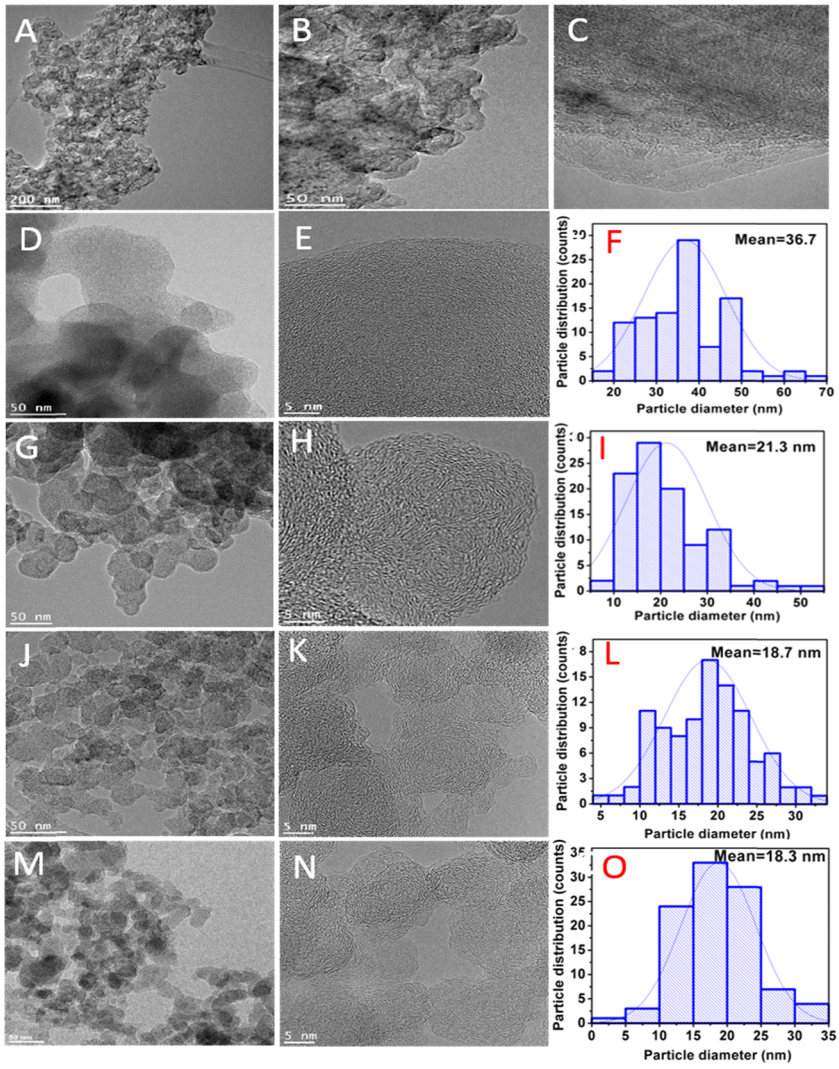

Figure 2. Aberration-corrected TEM images of samples acquired at low and high magnifications. The acquired images depict (A–C) graphite and nanostructures and primary particle size distribution of (D–F) DE soot, (G–I) DF soot, (J–L) JE soot, and (M–O) JF soot.

addition to diesel reduced the L_c and L_a values by 23 and 7%, respectively, in the engine and by 19 and 7%, respectively, in the flame. The percentage reductions in crystallite dimensions due to biodiesel addition to diesel in both the flame and engine setups were quite close and not notably different. Moreover, the average number of PAH layers in the nanocrystallites in diesel soots (DE and DF) was around 4, while on the other hand, it was around 3 for soots from blended fuel (JE and JF). The shorter crystallites in soots from the blended fuel are a result of reduced soot growth rate due to efficient hydrocarbon combustion and/or partial oxidation of soot during combustion. The shorter and curved (shown later through HRTEM analysis) PAHs in soot from blended fuel lead to smaller L_c that was also observed in ref 43.

3.3. High-Resolution Transmission Electron Microscopy (HRTEM). All of the soot samples derived from the flame and engine setups along with a graphite sample were subjected to HRTEM analysis. For consistency of imaging analysis, a sampling region under low magnification (at 200 and 100 nm scale) with maximum number of soot particle agglomerates (>100 particles) was identified. Several high-magnification and high-resolution images were recorded of many carbon particles by applying aberration correction during imaging. Figure 2 presents the HRTEM images recorded at the resolutions of 5 and 50 nm. Graphite does not have an agglomerate structure like soot, and therefore, no primary particle size could be measured. All soot samples exhibited high agglomeration and were composed of carbon spherules partly merged with the neighboring particles due to sintering effect. Each primary particle exhibits a typically oxidized and disordered core structure with highly curved fringes and relatively ordered graphitic layers along the periphery in the shell (see Figure 2F,I,L,O). On the contrary and as expected, the graphite sample completely lacks the core–shell structure and is composed of dense, long-range, ordered graphitic layers or fringes, as shown in Figure 2C. A detailed analysis of soot primary particle diameter of approximately 100 particles using ImageJ software and further analysis using Microsoft Excel obtained the kurtosis and skewness values. The observed values of kurtosis and skewness were in the range of −0.3 to 0.3 and −0.1 to 0.4, respectively, which suggested that the size distribution was close to the normal distribution. The mean particle diameters suggested that the primary particles were relatively bigger in the case of engine-generated soot samples, DE (36.7 nm) and JE (18.7 nm), compared to the corresponding flame-generated soot samples, DF (21.3 nm)

https://dx.doi.org/10.1021/acs.energyfuels.0c02063
Energy Fuels 2020, 34, 12960–12971

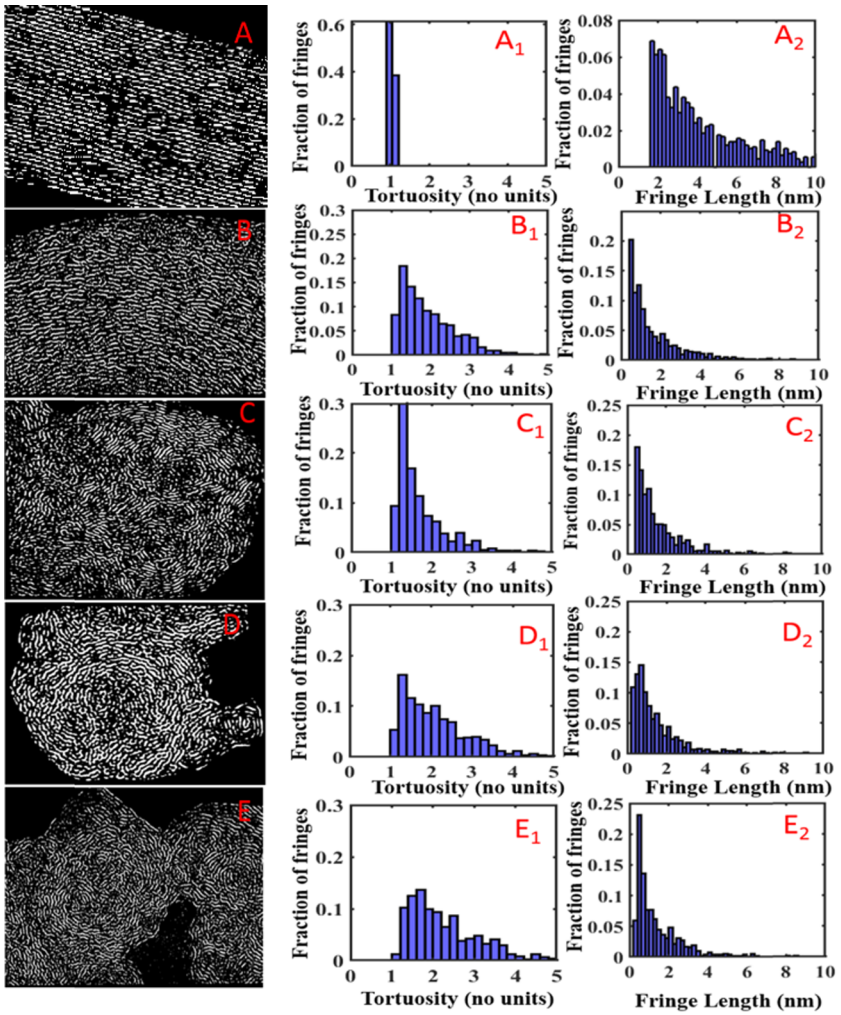

Figure 3. MATLAB-processed soot nanostructure analysis with corresponding tortuosity and fringe length distribution of graphite (A, A1, A2), DE soot (B, B1, B2), DF soot (C, C1, C2), JE soot (D, D1, D2), and JF soot (E, E1, E2).

and JF (18.3 nm). This is possibly because of the higher temperature and pressure in engine compared to flame setup, which results in greater sintering of the primary particles and higher condensation rate of PAHs on soot to increase their size.[44,45] Moreover, the difference between the mean primary particle diameters of JE and JF is lower than that of the DE and DF because, during the combustion of diesel with Jatropha biodiesel having fuel-bound oxygen in both the combustion environments, soot oxidation is enhanced, which competes with soot growth to keep the particle size relatively small, as observed in the literature.[14,22,46]

Furthermore, a MATLAB code, based on the algorithm reported in ref 47, was utilized to get quantitative information about the fringe length (L_a) and fringe tortuosity index. Each HRTEM image was subjected to negative transformation and grayscale conversion. The negative transformation is defined as $I_{negative} = L\text{-}1\text{-}I_{original}$, wherein $I_{original}$ is the image pixel value of images prior to transformation and L is the discrete intensity levels (minimum 256 per image). Several regions of interest (ROI) were operated with Gaussian filter, histogram equalization, and Tophat transformation to eliminate errors due to unequal illumination throughout the micrograph, which consequently improved the fringe contrast. Fringe skeletonization using parallel thinning algorithm[48] in the MATLAB code allowed eliminating branches from parent fringes so as to retain the longest possible fringes. The smallest branch was identified, and the branch connections were broken by setting the first pixel to this branch as zero. The detailed procedure, equations, and algorithms used are already listed in detail in ref 47, and hence not repeated here. From the TEM images with around 100 particles, five high-resolution microstructural images of each primary particle are randomly chosen having at least >100 fringe microstructures. The MATLAB image analysis of these provides the mean values of the fringe length and fringe tortuosity values (listed in Table 2). The analyzed fringe structures for all soots and graphite are shown in Figure 3.

The quantitative fringe structure analysis revealed that the graphite sample shows near-straight, long-range ordered fringes with a tortuosity index of 1.02 and a mean fringe length of 5.1 nm. On the contrary, all soot samples exhibited a greater degree of fringe curvature and shorter fringe lengths. The fringe length in DE was only marginally smaller than that in DF, thus following qualitatively the same trend as XRD results. However, the fringe lengths from HRTEM were smaller compared to L_a values from XRD possibly due to uneven contrast in HRTEM images that can lead to a fringe being unintentionally broken down into smaller fringes during MATLAB processing. The fringe tortuosity was greater in flame soot compared to engine soot. The differences in the

https://dx.doi.org/10.1021/acs.energyfuels.0c02063
Energy Fuels 2020, 34, 12960−12971

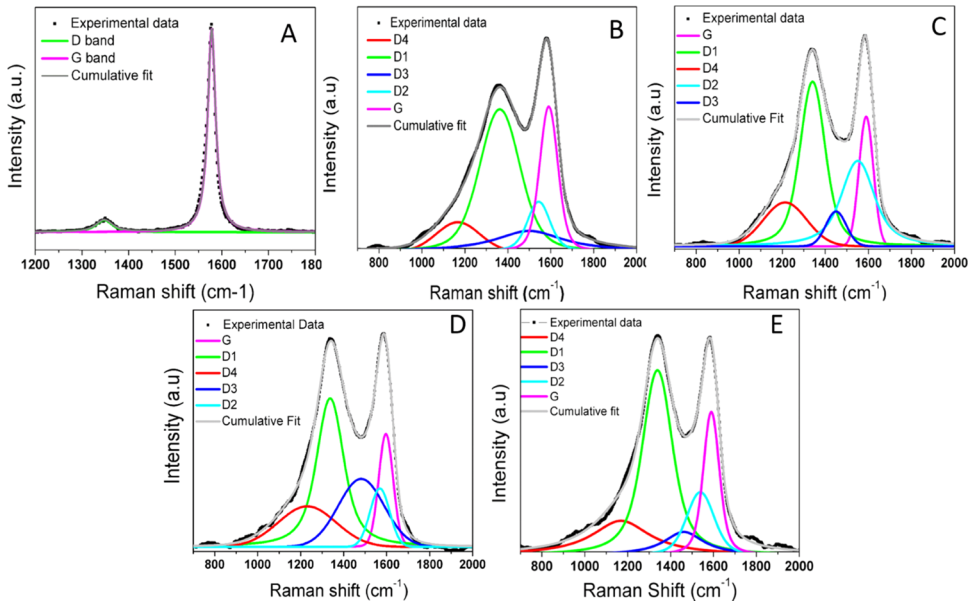

Figure 4. Raman spectra of (A) graphite, (B) DE soot, (C) DF soot, (D) JE soot, and (E) JF soot.

crystallite structure parameters of engine and flame soots (DE-DF or JE-JF) could well be due to excess oxygen and higher pressure and temperature in engines that may be supporting planar PAH formation over curved ones or would be eliminating the curved ones that are more reactive than planar ones.[49] The effect of combustor operating conditions on curved PAH chemistry is not well understood, and it is still an active area of research.[50−52]

The addition of Jatropha biodiesel to diesel enhances soot oxidation, resulting in a reduction in the fringe length and an increase in tortuosity in soot from blended fuel compared to diesel soot. An increase in tortuosity is a result of partial oxidation of PAHs in soot, where the oxidation of a six-membered aromatic ring forms a five-membered ring that introduces curvature in their structure.[49,53] A similar observation was made in refs 25, 43, where the presence of fuel-bound oxygen (and increased oxygen:fuel ratio) induced greater internal oxidation in soot.

The crystallite length (fringe length), found through HRTEM image analysis, is lower than that found through XRD analysis in Table 2, though the difference is less than some similar studies.[14,34] Aberration correction can be a reason for it, as it significantly reduces the circle of least confusion arising from the spherical aberration of the lens, and thus enhances image quality and resolution and reduces blur. This further improves the image processing in Matlab to provide more accurate estimation of crystal structure parameters. It is expected that HRTEM would underpredict crystal structure parameters due to the unavoidable projection error (since the incident beam is not always at 90° for all of the fringes, and imaging a fringe from an angle different from 90° would reduce its projected length). Moreover, the recorded area in XRD is near 50μ × 50μ, while is it is near 250 nm × 250 nm (or lower depending on the desired resolution). Thus, XRD is expected to provide a better estimate of crystallite parameters than HRTEM. However, both the techniques predicted similar trends qualitatively.

3.4. Raman Spectroscopy. Raman spectroscopy is a useful technique to analyze soot nanostructure, especially because, unlike XRD, it can provide information about the amorphous carbon content in soot. The disordered carbon structure exhibits Raman signals in the region of 900−2000 cm^{-1}, as presented in Figure 4 for the four soot samples and the graphite reference sample. The graphite sample has the characteristic high-intensity and sharp peak at 1590 cm^{-1}, called the graphitic peak (G), which represents a highly ordered structure made up of graphene layers, while the crystal defects are represented by a very low intensity peak at 1350 cm^{-1}. Unlike the graphite sample, the Raman spectra of all soot samples exhibited low-intensity broad bands, centering at 1350 and at 1590 cm^{-1}. The increase in the intensity of the D bands relative to the G band in these Raman spectra is a result of enhanced crystal disorder.[46,54]

The broad-band structure is further deconvoluted via a five-peak fitting model using the Voight function,[55] as shown in Figure 4B−E. The corresponding fitted peaks are described as D1 = 1350 cm^{-1}, D2 = 1560 cm^{-1}, D3 = 1445 cm^{-1}, D4 = 1220 cm^{-1}, and G =1590 cm^{-1}. The lattice vibrations from disordered graphene layers and the amorphous carbon from organic functionalities are represented by D2 and D3, respectively. D4 represents the C−C bonds of polyene-like structures. The ratio of peak intensities (I_{D1}/I_G) is a good measure of the crystal structure disorder in soot samples, and it is related to the lattice width (L_a) through Knight and White eq EE4.[56]

$$L_a = 4.4\left(\frac{I_{D1}}{I_G}\right)^{-1} \quad \text{(E4)}$$

As evident from Table 2, the ratio of I_{D1}/I_G is higher in the flame soots compared to engine soots for both the fuels, indicating less orderly structure in the former than the latter. As an alternative, the ratio of the peak areas of D1 and G curves was also calculated for comparison for each soot sample, and it was found to be 1.61 for DE, 2.04 for DF, 2.50 for JE, and 2.58 for JF soot samples. This trend is in good agreement with the ratio of peak intensity values (I_{D1}/I_G) reported in Table 2.

As expected, the trend is similar to that depicted by L_c values from XRD analysis. The DE soot exhibited an intense G band

https://dx.doi.org/10.1021/acs.energyfuels.0c02063
Energy Fuels 2020, 34, 12960−12971

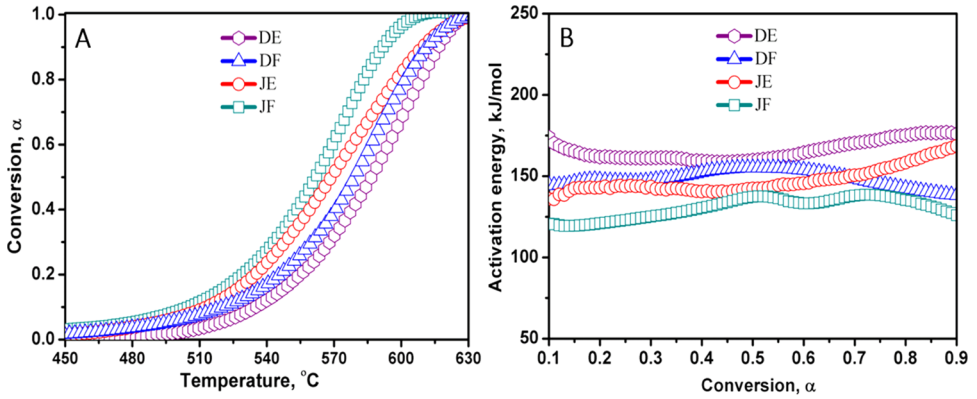

Figure 5. (A) Soot conversion profiles as a function of temperature and (B) variation in activation energy as a function of soot conversion measured through TGA experiments.

and a significantly lower D band with a lower I_{D1}/I_G ratio compared to DF soot. This is a result of increased graphitization and ordering in soot produced in an engine at higher pressure and temperature than a flame. The I_{D1}/I_G ratios of JE and JF soots also follow a similar trend, although the extent of disorder is significantly higher compared to DE and DF. The calculated values of lattice width, L_a, followed the same trend as that of L_a found from XRD analysis, with engine soots having higher L_a values than flame soots, which is already explained before. Through Raman analysis in a recent study,[57] it was observed that an increase in combustion pressure increases L_a values in soot, which is in line with the results found here for flame and engine soots. The Jatropha biodiesel-blended diesel soot has a lower L_a and a higher I_{D1}/I_G ratio (disordered structure) than diesel soot as a result of enhanced internal oxidation of soot catalyzed by the fuel-bound oxygen, which is in agreement with refs 25, 58.

The differences in the calculated values of L_a from Raman and XRD analysis could be due to the fact that, in XRD, only the signals corresponding to crystalline carbon aggregates were detected, while in the case of Raman spectroscopy, even the amorphous and disordered carbon contributes to the signal intensity, which represents the analysis of the bulk structure of soot.

3.5. Thermogravimetric Analysis (TGA). TGA serves as one of the most useful techniques for the integral analysis of soot oxidative reactivity and its oxidation kinetics. Such a study is crucial for estimating the soot oxidation rate and regeneration efficiency of diesel particulate filters. Typically, the soot conversion $(\alpha) = \frac{(M_o - M_T)}{(M_o - M_L)}$ is measured as a function of temperature at heating rates of 1, 3, 5, and 7 °C/min. M_o, M_T, and M_L represent initial soot mass, partially oxidized soot mass, and leftover soot mass (mainly, ash), respectively. The activation energy of soot oxidation is then calculated using the Friedman method.[59] The rate of soot conversion $\left(\frac{d\alpha}{dt}\right)$ and soot conversion (α) are related through eq EE5

$$\frac{d\alpha}{dt} = k(T)f(\alpha) \tag{E5}$$

wherein $k(T)$ is the soot oxidation rate constant obeying Arrhenius equation, $k = A\,e^{-E_a/RT}$. Here the preexponential factor, activation energy, and the temperature of soot oxidation are denoted as A, E_a, and T, respectively.[60] The conversion function, $f(\alpha)$, represents the overall reaction model, which avoids the need for detailed individual oxidation reactions. Equation EE5 can be represented in a logarithmic form as

$$\ln\left(\frac{d\alpha}{dt}\right)_{\alpha,i} = -\frac{E_\alpha}{RT_{\alpha,i}} + \ln[A(f(\alpha))]_{\alpha,i} \tag{E5.1}$$

wherein i varying from 1 to 4 is representative of the experimental results that correspond to the heating rate of $(2i - 1)$ °C/min, and E_α and $T_{\alpha,i}$ represent the activation energy and the temperature corresponding to a given α, respectively. The slope of the plot of $\ln(d\alpha/dt)_{\alpha,i}$ vs $1/T_{\alpha,I}$ at a given conversion gives the E_a value for soot oxidation. The plot of soot conversion and soot conversion rates as a function of temperature and different heating rates is presented in Figure S2 in the Supporting Information. Figure S3 in the Supporting Information presents the plots of eq EE5.1.E5.1, from which activation energies were obtained. The term $\ln [A(f(\alpha))]_{\alpha,i}$ in eq EE5.1.E5.1 includes important information related to the preexponential factor (A) and the soot oxidation model, and can convey some information related to entropy of activation (entropy difference between the reactants and the transition state) for the rate-determining step during soot oxidation. Therefore, this term was calculated and is plotted in Figures S4 and S5 in the Supporting Information. A discussion on the entropy of activation and its relation to the observed reactivity trend is also provided in the Supporting Information. More details about the procedure for activation energy calculation using the soot conversion profiles at different heating rates can be found in refs 60, 61. A more accurate estimation of activation energy would be based on a detailed combustion kinetic model of fuels/soots, but such combustion models are extremely complex with a large number of reactions and chemical species, many of which are radicals and undergo fast reactions. Moreover, in a given TGA experiment at a fixed heating rate, the temperature gradient between the sample holder and soot sample also has an effect on the soot conversion profile in a dynamic system that is difficult to model accurately. While the above-discussed method of calculating activation energy considers some artifacts in the results due to the temperature gradient by estimating soot conversions at different heating rates (e.g., fast heating rates such as 5 and 7 °C/min ensure that the temperature gradient effects are minimum and the oxidation chemistry of soot governs the observed trends in activation energy), it is still possible that the observed variations in activation energy with time could be a result of: (a) experimental artifacts such as the

https://dx.doi.org/10.1021/acs.energyfuels.0c02063
Energy Fuels 2020, 34, 12960−12971

temperature gradient in the sample and the gas phase and the mass transfer limitations in the penetration of O_2 molecules in the core of soot samples that are difficult to model, and (b) the model assumption that soot oxidation would follow eqs EE5 and EE5.1.E5.1 to be able to use Friedman method for determining activation energy. Therefore, as per the recommendations of ICTAC Kinetics Committee for kinetic computations on thermal analysis data,[61] the complex detailed reaction models are avoided and are replaced by a global kinetic model represented by f(α) so that global activation energies can be estimated, which have been very useful in predicting oxidative reactivity of soots.

Typically, a shift in the soot conversion curve toward higher temperatures is observed, as the heating rate is increased. This is a result of (a) temperature gradient between the soot sample and the air due to heat transfer delay. (b) As the heating rate is increased, the time available for soot to reach a given temperature and get oxidized by O_2 at that temperature reduces. This reaction delay causes the same soot conversion level to be achieved at a higher temperature with a higher heating rate. By performing TGA experiments at different heating rates, a cumulative analysis of all possible effects of time delays and reactivity of soot with O_2 can be accounted for, thus allowing a more accurate estimation of global activation energy.[62] Figure 5A presents the typical soot conversion (α) as a function of temperature measured at a constant heating rate of 5 °C/min.

As evident from Figure 5A, 10% conversion of DE and DF soots occurs at temperatures of 535 and 520 °C, while JE and JF soots need relatively lower oxidation temperatures of 512 and 503 °C, respectively. The conversion of 50% for DE and DF soots occurs at 587 and 579 °C, while that for JE and JF occurs at 569 and 562 °C, respectively. At a stage near complete oxidation, i.e., 90% conversion, DE and DF need 617 and 612 °C, while 608 and 592 °C are needed for JE and JF soots, respectively. This clearly shows that the differences in the soot nanostructural characteristics such as lower primary particle size, higher tortuosity, and smaller fringe length, as observed in XRD and HRTEM analyses, especially in the case of Jatropha biodiesel-blended diesel soot, result in enhanced oxidation of soot structure at a relatively lower temperature. Figure 5B depicts the variation in activation energy as a function soot conversion. The initial activation energy serves as a good indicator of the soot nanostructural reactivity and its ease of oxidation with O_2. As evident from Figure 5B, DE soot has the highest initial activation energy of ~170 ±10 kJ/mol, while JF has the least value of ~123 ± 10 kJ/mol. The difference in the activation energies of engine- and flame-generated diesel soots (DF and DE) is around 30 kJ/mol, while the activation energy of Jatropha biodiesel-blended diesel engine soot (130 ± 10 kJ/mol) is 7 kJ/mol higher than that of flame-generated soot. This suggests that engine-generated soots are relatively difficult to oxidize due to their enhanced graphitic character and lower nanostructural disorder, as observed in Raman and HRTEM analyses. The lower difference in activation energies between flame and engine soots with the biodiesel-blended fuel implies that the enhanced soot oxidation due to fuel-bound oxygen with Jatropha biodiesel possibly surpasses the soot formation rate, the effect of which partially compensates for the differences in engine and flame combustion conditions. This observation is consistent with the earlier observations regarding soot nanostructural characteristics in Table 2.

3.6. Electron Energy Loss Spectroscopy (EELS). The EELS technique proves to be effective in obtaining the information about the atomic structure of carbons in soot. In this method, the energy loss that occurs during the inelastic collision of an electron beam with that of orbital electrons of carbon in soot is measured. Typically, two electronic bands, one around 285−287 eV, called the π^* band, and the other near 290−305 eV, called the σ^* band, are observed, as shown in Figure 6. A qualitative comparison of the π^* and σ^* intensity values of graphite with that of soot samples shows a critical difference in the relative peak intensity and the shape of the peaks. In the case of graphite, the π^* peak is more intense and well resolved compared to the σ^* band intensity, confirming that the sp^2 character is prominent due to the presence of C=C in the graphene layers. On the contrary, the π^* intensity is much lower than the σ^* band in all of the soot samples, confirming a greater degree of crystal structure disorder and an increased sp^3 character due to surface functionalities in combustion-generated soots. Therefore, the π^* peak intensity provided an estimate of the sp^2 character of the carbon bonds present in the soot structure. Initially, the sp^2 content (R) of the soot sample is calculated as

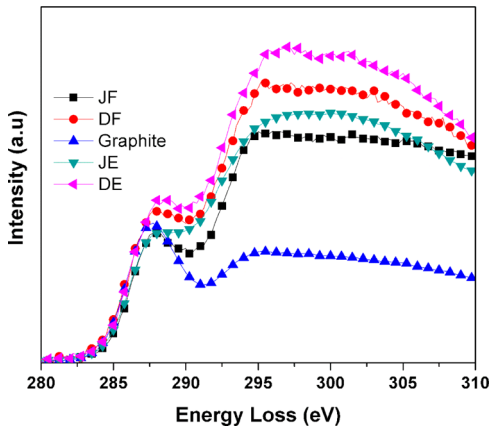

Figure 6. EELS spectra of graphite, diesel soot (DE and DF), and Jatropha biodiesel-blended diesel soot (JE and JF) generated using engine and flame.

$$R = \frac{I_k(\pi^*)I_l(\Delta)}{I_k(\Delta)I_0} \quad \text{(E6)}$$

wherein the K shell intensity of π^* peak is denoted as $I_k(\pi^*)$, while the K-loss integrated throughout the energy range Δ (=50 eV) beginning at the threshold is denoted as $I_k(\Delta)$. The ratio $I_l(\Delta)/I_0$ represents low-loss and zero-loss intensities, which are used to correct for plural scattering existing in $I_k(\Delta)$. Subsequently, the percentage of sp^2 carbons in the soot sample is calculated with respect to the sp^2 content of the graphite sample (R_g) as follows

$$f = \frac{R}{R_g} \times 100 \quad \text{(E7)}$$

The quantitative values determined from the above analysis are presented below. The DE and DF soots have around 61 and 57% sp^2 character, respectively, while JE and JF soots have 47 and 39% sp^2 character, respectively. It is to be noted that the engine soots, DE and JE, have relatively greater sp^2 character compared to their counterparts, DF and JF, generated from

https://dx.doi.org/10.1021/acs.energyfuels.0c02063
Energy Fuels 2020, 34, 12960−12971

flame, due to the relatively increased graphitization effect of carbon structure in the engine environment, which is in good agreement with the results obtained from Raman analysis. Moreover, the diesel soots from engine and flame setups show significantly higher sp^2 character (more graphitized) than the Jatropha-blended diesel soots. With addition of neem biodiesel to diesel, a decrease in sp^2/sp^3 ratio was also reported in ref 34 through EELS analysis. On the contrary, an investigation by Song et al.[63] on soot particles from Fischer−Tropsch fuel and pure soybean biodiesel using EELS spectroscopy concluded that pure biodiesel soot was more ordered with higher sp^2 character compared to the Fischer−Tropsch fuel soot. The effect of biodiesel was probably substantially reduced in our soot samples, as we did not use 100% biodiesel to replace diesel in engine, but only 20% Jatropha biodiesel was blended with diesel. Nonetheless, the higher oxidative reactivity, the lower sp^2 character, and PAH stacks of smaller lengths and greater interplanar separation (as observed in previous sections) point toward the presence of aliphatics (that are more reactive than aromatics) on soot from biodiesel/diesel blend, which is possibly induced by the addition of oxygen/OH/hydrocarbon radical species on the PAH layers at the edge carbon atoms.[14]

Based on the above studies, it is observed that atmospheric-pressure flame setup in smoke point apparatus is able to qualitatively predict the fuel effects on the physical and chemical characteristics of soot particles that were observed in engine, although some differences were found quantitatively due to higher pressure, temperature, and oxygen content in engine compared to a sooting diffusion flame.

4. CONCLUSIONS

A series of detailed nonstructural characterization tests and comparisons between soots obtained from diesel and Jatropha biodiesel/diesel blend obtained via engine and flame setups were conducted. Two sets of soot for each fuel blend were generated using an ASTM standard smoke point flame apparatus and a four-stroke, single-cylinder diesel engine. A striking difference between soots from these two combustors was found through XRD analysis, where engine soots had a high concentration of loosely bound aliphatic hydrocarbons, although they tend to detach from soot easily when heated at merely 300 °C, far below the oxidation temperature of diesel soot. It was due to high fuel flow rates in engines than in flames that increase the unburned hydrocarbon concentration per unit time to adsorb on soot during collection. In general, engine soots exhibited greater graphitic character than flame soots due to the graphitization effect under engine conditions of high temperature and pressure. The overall trend in soot nanostructural analysis by HRTEM, XRD, Raman, TGA, and EELS analyses suggests that engine soots have greater primary particle diameter, lower interplanar separation, greater PAH stack dimensions, lower fringe tortuosity, lower oxidative reactivity (higher activation energy), and higher sp^2 character than the flame soots (though the differences in some parameters such as interplanar separation, crystallite length, thickness, and tortuosity were minor, and could be considered to be similar). However, no difference in the trend prediction was found irrespective of the combustion setup (flame and engine), when a biodiesel was blended with diesel. For example, in both flame and engine, the addition of biodiesel to diesel reduced particle size, increased interlayer spacing, reduced crystallite dimensions (i.e., reduced graphitic character), increased tortuosity, reduced sp^2 character, and enhanced soot reactivity. Moreover, biodiesel addition to diesel also reduced the differences observed between flame soot and engine soot, which indicates that, in less sooting conditions, flame and engine soots appear more similar to each other. The oxidative reactivity trend in TGA agreed well with the above changes in soot nanostructures. The results suggest that, while engine soot nanostructure has more relevance to the actual anthropogenic particulate matter, the smoke point apparatus appears to be an economical and suitable tool for studying the effect of an additive/blending component to diesel on the soot physicochemical properties and soot reduction potential, and can be helpful to screen fuel additives before utilizing them for engine applications.

■ ASSOCIATED CONTENT

Supporting Information

The Supporting Information is available free of charge at https://pubs.acs.org/doi/10.1021/acs.energyfuels.0c02063.

Schematic of the flame and engine setups, a table containing engine parameters, and calculations related to the calorific value and flash point of the fuels (PDF)

■ AUTHOR INFORMATION

Corresponding Author

Abhijeet Raj − *Department of Chemical Engineering and Centre for Catalysis and Separation, Khalifa University of Science & Technology, Abu Dhabi 127788, U.A.E.*; orcid.org/0000-0002-1470-0513; Phone: +971-26075738; Email: abhijeet.raj@ku.ac.ae

Authors

Pranay P. Morajkar − *Department of Chemical Engineering, Khalifa University of Science & Technology, Abu Dhabi 127788, U.A.E.; School of Chemical Sciences, Goa University, Goa 403206, India*; orcid.org/0000-0002-2602-6183

Moataz K. Abdrabou − *Department of Chemical Engineering, Khalifa University of Science & Technology, Abu Dhabi 127788, U.A.E.*

Akshay V. Salkar − *School of Chemical Sciences, Goa University, Goa 403206, India*

Mirella Elkadi − *Department of Chemistry, Khalifa University of Science & Technology, Abu Dhabi 127788, U.A.E.*

Dalaver H. Anjum − *Department of Physics and Centre for Catalysis and Separation, Khalifa University of Science & Technology, Abu Dhabi 127788, U.A.E.*

Complete contact information is available at: https://pubs.acs.org/10.1021/acs.energyfuels.0c02063

Notes

The authors declare no competing financial interest.

■ ACKNOWLEDGMENTS

The authors acknowledge the financial support received from Khalifa University of Science & Technology (CIRA-2018-99), UAE, and instrumental facilities support of Goa University, India (via DST/IMRCD/INNO-INDIGO/BioCFD/2017(G)), to accomplish this work. This publication is based upon work supported by Khalifa University of Science and Technology under Award No. RC2-2018-024.

REFERENCES

(1) Maione, M.; Fowler, D.; Monks, P. S.; Reis, S.; Rudich, Y.; Williams, M. L.; Fuzzi, S. Air quality and climate change: Designing new win-win policies for Europe. *Environ. Sci. Policy* **2016**, *65*, 48−57.

(2) Amedro, D.; Parker, A. E.; Schoemaecker, C.; Jain, C.; Morajkar, P.; Monks, P. S.; Miyazaki, K.; Kajii, Y.; Fittschen, C. *HOx and ROx Radicals in Atmospheric Chemistry, Disposal of Dangerous Chemicals in Urban Areas and Mega Cities, Dordrecht*; Barnes, I.; Rudziński, K. J., Eds.; Springer: Dordrecht, Netherlands, 2013; pp 77−92.

(3) Yuan, X.; Liu, H.; Gao, Y. Diesel Engine SCR Control: Current Development and Future Challenges. *Emiss. Control Sci. Technol.* **2015**, *1*, 121−133.

(4) Wang, Y.; Chung, S. H. Soot formation in laminar counterflow flames. *Prog. Energy Combust. Sci.* **2019**, *74*, 152−238.

(5) Peña, G. D. G.; Pillai, V.; Raj, A.; Brito, J. L. Effects of fuel-bound methyl groups and fuel flow rate in the diffusion flames of aromatic fuels on the formation of volatile PAHs. *Combust. Flame* **2018**, *198*, 412−427.

(6) Ramanathan, V.; Carmichael, G. Global and regional climate changes due to black carbon. *Nat. Geosci.* **2008**, *1*, 221−227.

(7) Agency USEP. Regulatory Actions, 2015. https://www3.epa.gov/pm/actions.html (accessed June 20, 2020).

(8) Rodríguez-Fernández, J.; Lapuerta, M.; Sánchez-Valdepeñas, J. Regeneration of diesel particulate filters: Effect of renewable fuels. *Renewable Energy* **2017**, *104*, 30−39.

(9) Lapuerta, M.; Rodríguez-Fernández, J.; Sánchez-Valdepeñas, J. Soot reactivity analysis and implications on diesel filter regeneration. *Prog. Energy Combust. Sci.* **2020**, *78*, No. 100833.

(10) Park, S. H.; Cha, J.; Lee, C. S. Effects of Bioethanol-Blended Diesel Fuel on Combustion and Emission Reduction Characteristics in a Direct-Injection Diesel Engine with Exhaust Gas Recirculation (EGR). *Energy Fuels* **2010**, *24*, 3872−3883.

(11) Chukwuezie, O. C.; Nwaigwe, K. N.; Asoegwu, S. N.; Anyanwu, E. E. Diesel engine performance of jatropha biodiesel: a review. *Biofuels* **2014**, *5*, 415−430.

(12) Chauhan, B. S.; Kumar, N.; Cho, H. M.; Lim, H. C. A study on the performance and emission of a diesel engine fueled with Karanja biodiesel and its blends. *Energy* **2013**, *56*, 1−7.

(13) Hussain, A.; Mehdi, S. M.; Akhtar, M.; Ani, F. N.; Ahmed, I. Combustion Performance of Diesel Palm Olein Fuel: A Combined CFD and Experimental Approach. *Arabian J. Sci. Eng.* **2018**, *43*, 1291−1300.

(14) Morajkar, P. P.; Guerrero Peña, G. D. J.; Raj, A.; Elkadi, M.; Rahman, R. K.; Salkar, A. V.; Pillay, A.; Anjana, T.; Cha, M. S. Effects of Camphor Oil Addition to Diesel on the Nanostructures and Oxidative Reactivity of Combustion-Generated Soot. *Energy Fuels* **2019**, *33*, 12852−12864.

(15) Rodríguez-Fernández, J.; Hernández, J. J.; Sánchez-Valdepeñas, J. Effect of oxygenated and paraffinic alternative diesel fuels on soot reactivity and implications on DPF regeneration. *Fuel* **2016**, *185*, 460−467.

(16) Lapuerta, M.; Rodríguez-Fernández, J.; Sánchez-Valdepeñas, J.; Salgado, M. S. Multi-Technique Analysis of Soot Reactivity from Conventional and Paraffinic Diesel Fuels. *Flow, Turbul. Combust.* **2016**, *96*, 327−341.

(17) Yehliu, K.; Armas, O.; Vander Wal, R. L.; Boehman, A. L. Impact of engine operating modes and combustion phasing on the reactivity of diesel soot. *Combust. Flame* **2013**, *160*, 682−691.

(18) Ruiz, F. A.; Cadrazco, M.; López, A. F.; Sanchez-Valdepeñas, J.; Agudelo, J. R. Impact of dual-fuel combustion with n-butanol or hydrous ethanol on the oxidation reactivity and nanostructure of diesel particulate matter. *Fuel* **2015**, *161*, 18−25.

(19) Braun, A.; Shah, N.; Huggins, F. E.; Kelly, K. E.; Sarofim, A.; Jacobsen, C.; Wirick, S.; Francis, H.; Ilavsky, J.; Thomas, G. E.; Huffman, G. P. X-ray scattering and spectroscopy studies on diesel soot from oxygenated fuel under various engine load conditions. *Carbon* **2005**, *43*, 2588−2599.

(20) Yehliu, K.; Lilik, G. K.; Vander Wal, R. L.; Sun, C.; Boehman, A. L. Impacts of advanced diesel combustion operation on soot nanostructure and reactivity. *Int. J. Engine Res.* **2017**, *18*, 532−542.

(21) Parent, P.; Laffon, C.; Marhaba, I.; Ferry, D.; Regier, T.; Ortega, I.; Chazallon, B.; Carpentier, Y.; Focsa, C. Nanoscale characterization of aircraft soot: A high-resolution transmission electron microscopy, Raman spectroscopy, X-ray photoelectron and near-edge X-ray absorption spectroscopy study. *Carbon* **2016**, *101*, 86−100.

(22) Lapuerta, M.; Oliva, F.; Agudelo, J. R.; Boehman, A. L. Effect of fuel on the soot nanostructure and consequences on loading and regeneration of diesel particulate filters. *Combust. Flame* **2012**, *159*, 844−853.

(23) Xu, Z.; Li, X.; Guan, C.; Huang, Z. Effects of injection timing on exhaust particle size and nanostructure on a diesel engine at different loads. *J. Aerosol Sci.* **2014**, *76*, 28−38.

(24) Verma, P.; Jafari, M.; Guo, Y.; Pickering, E.; Stevanovic, S.; Bodisco, T. A.; Fernando, J. F.; Golberg, D.; Brooks, P.; Brown, R. Experimental analysis of the morphology and nanostructure of soot particles for butanol/diesel blends at different engine operating modes. *Energy Fuels* **2019**, *33*, 5632−5646.

(25) Man, X.; Cheung, C.; Ning, Z.; Yung, K. Effect of waste cooking oil biodiesel on the properties of particulate from a DI diesel engine. *Aerosol Sci. Technol.* **2015**, *49*, 199−209.

(26) McEnally, C. S.; Pfefferle, L. D. Improved sooting tendency measurements for aromatic hydrocarbons and their implications for naphthalene formation pathways. *Combust. Flame* **2007**, *148*, 210−222.

(27) Crossley, S. P.; Alvarez, W. E.; Resasco, D. E. Novel micropyrolyis index (mpi) to estimate the sooting tendency of fuels. *Energy Fuels* **2008**, *22*, 2455−2464.

(28) Calcote, H.; Manos, D. Effect of molecular structure on incipient soot formation. *Combust. Flame* **1983**, *49*, 289−304.

(29) Maricq, M. M. Examining the Relationship Between Black Carbon and Soot in Flames and Engine Exhaust. *Aerosol Sci.Technol.* **2014**, *48*, 620−629.

(30) ASTM D975-15b. *Standard Specification for Diesel Fuel Oils*; ASTM International: West Conshohocken, PA, 2015. www.astm.org.

(31) Alrefaai, M. M.; Peña, G. D. G.; Raj, A.; Stephen, S.; Anjana, T.; Dindi, A. Impact of dicyclopentadiene addition to diesel on cetane number, sooting propensity, and soot characteristics. *Fuel* **2018**, *216*, 110−120.

(32) Peña, G. D. G.; Alrefaai, M. M.; Yang, S. Y.; Raj, A.; Brito, J. L.; Stephen, S.; Anjana, T.; Pillai, V.; Al Shoaibi, A.; Chung, S. H. Effects of methyl group on aromatic hydrocarbons on the nanostructures and oxidative reactivity of combustion-generated soot. *Combust. Flame* **2016**, *172*, 1−12.

(33) Peña, G. D.; Rahman, R. K.; Raj, A.; Stephen, S.; Anjana, T.; Brito, J. L. Effect of fuel flow rate on the characteristics of soot generated from unsubstituted and disubstituted aromatic hydrocarbon flames: Experimental and numerical study. *Combust. Flame* **2018**, *190*, 224−239.

(34) Kareem, M. O.; Pena, G. D. J. G.; Raj, A.; Alrefaai, M. M.; Stephen, S.; Anjana, T. Effects of Neem Oil-Derived Biodiesel Addition to Diesel on the Reactivity and Characteristics of Combustion-Generated Soot. *Energy Fuels* **2017**, *31*, 10822−10832.

(35) Kousoulidou, M.; Ntziachristos, L.; Fontaras, G.; Martini, G.; Dilara, P.; Samaras, Z. Impact of biodiesel application at various blending ratios on passenger cars of different fueling technologies. *Fuel* **2012**, *98*, 88−94.

(36) Erni, R. *Aberration-Corrected Imaging in Transmission Electron Microscopy: An Introduction*, 2nd ed.; World Scientific Publishing Company, 2015.

(37) Zhou, J.; Anjum, D. H.; Lubineau, G.; Li, E. Q.; Thoroddsen, S. T. Unraveling the order and disorder in poly (3, 4-ethylenedioxythiophene)/poly (styrenesulfonate) nanofilms. *Macromolecules* **2015**, *48*, 5688−5696.

(38) Datta, A.; Palit, S.; Mandal, B. K. An experimental study on the performance and emission characteristics of a CI engine fuelled with

https://dx.doi.org/10.1021/acs.energyfuels.0c02063
Energy Fuels 2020, 34, 12960−12971

Jatropha biodiesel and its blends with diesel. *J. Mech. Sci. Technol.* **2014**, *28*, 1961−1966.
(39) Lu, L.; Sahajwalla, V.; Kong, C.; Harris, D. Quantitative X-ray diffraction analysis and its application to various coals. *Carbon* **2001**, *39*, 1821−1833.
(40) Fujimoto, H. Theoretical X-ray scattering intensity of carbons with turbostratic stacking and AB stacking structures. *Carbon* **2003**, *41*, 1585−1592.
(41) Yang, Y.; Boehman, A. L.; Santoro, R. J. A study of jet fuel sooting tendency using the threshold sooting index (TSI) model. *Combust. Flame* **2007**, *149*, 191−205.
(42) Marsh, H. A tribute to Philip L. Walker. *Carbon* **1991**, *29*, 703−704.
(43) Yehliu, K.; Vander Wal, R. L.; Armas, O.; Boehman, A. L. Impact of fuel formulation on the nanostructure and reactivity of diesel soot. *Combust. Flame* **2012**, *159*, 3597−3606.
(44) Lu, T.; Cheung, C.; Huang, Z. Size-resolved volatility, morphology, nanostructure, and oxidation characteristics of diesel particulate. *Energy Fuels* **2012**, *26*, 6168−6176.
(45) Lapuerta, M.; Martos, F. J.; Herreros, J. M. Effect of engine operating conditions on the size of primary particles composing diesel soot agglomerates. *J. Aerosol Sci.* **2007**, *38*, 455−466.
(46) Salamanca, M.; Mondragón, F.; Agudelo, J. R.; Benjumea, P.; Santamaría, A. Variations in the chemical composition and morphology of soot induced by the unsaturation degree of biodiesel and a biodiesel blend. *Combust. Flame* **2012**, *159*, 1100−1108.
(47) Yehliu, K.; Vander Wal, R. L.; Boehman, A. L. Development of an HRTEM image analysis method to quantify carbon nanostructure. *Combust. Flame* **2011**, *158*, 1837−1851.
(48) Lam, L.; Lee, S.-W.; Suen, C. Y. Thinning methodologies-a comprehensive survey. *IEEE Trans. Pattern Anal. Mach. Intell.* **1992**, *14*, 869−885.
(49) Raj, A.; Yang, S. Y.; Cha, D.; Tayouo, R.; Chung, S. H. Structural effects on the oxidation of soot particles by O2: Experimental and theoretical study. *Combust. Flame* **2013**, *160*, 1812−1826.
(50) Raj, A. Structural effects on the growth of large polycyclic aromatic hydrocarbons by C2H2. *Combust. Flame* **2019**, *204*, 331−340.
(51) Martin, J. W.; Menon, A.; Lao, C. T.; Akroyd, J.; Kraft, M. Dynamic polarity of curved aromatic soot precursors. *Combust. Flame* **2019**, *206*, 150−157.
(52) Martin, J. W.; Bowal, K.; Menon, A.; Slavchov, R. I.; Akroyd, J.; Mosbach, S.; Kraft, M. Polar curved polycyclic aromatic hydrocarbons in soot formation. *Proc. Combust. Inst.* **2019**, *37*, 1117−1123.
(53) Chaparala, S. V.; Raj, A. Reaction mechanism for the oxidation of zigzag site on polycyclic aromatic hydrocarbons in soot by O2. *Combust. Flame* **2016**, *165*, 21−33.
(54) Sadezky, A.; Muckenhuber, H.; Grothe, H.; Niessner, R.; Pöschl, U. Raman microspectroscopy of soot and related carbonaceous materials: spectral analysis and structural information. *Carbon* **2005**, *43*, 1731−1742.
(55) Catelani, T.; Pratesi, G.; Zoppi, M. Raman characterization of ambient airborne soot and associated mineral phases. *Aerosol Sci. Technol.* **2014**, *48*, 13−21.
(56) Escribano, R.; Sloan, J.; Siddique, N.; Sze, N.; Dudev, T. Raman spectroscopy of carbon-containing particles. *Vib. Spectrosc.* **2001**, *26*, 179−186.
(57) Commodo, M.; Karataş, A. E.; De Falco, G.; Minutolo, P.; D'Anna, A.; Gülder, Ö. L. On the effect of pressure on soot nanostructure: A Raman spectroscopy investigation. *Combust. Flame* **2020**, *219*, 13−19.
(58) Morajkar, P. P.; Abdrabou, M. K.; Raj, A.; Elkadi, M.; Stephen, S.; Ali, M. I. Transmission of trace metals from fuels to soot particles: An ICP-MS and soot nanostructural disorder study using diesel and diesel/Karanja biodiesel blend. *Fuel* **2020**, *280*, No. 118631.
(59) Friedman, H. L. Kinetics of thermal degradation of char-forming plastics from thermogravimetry. Application to a phenolic plastic. *J. Polym. Sci., Part C: Polym. Symp.* **1964**, 183−195.
(60) Elder, J. P. Reconciliation of Arrhenius and iso-conversional analysis kinetics parameters of non-isothermal data. *Thermochim. Acta* **1996**, *272*, 41−48.
(61) Vyazovkin, S.; Burnham, A. K.; Criado, J. M.; Pérez-Maqueda, L. A.; Popescu, C.; Sbirrazzuoli, N. ICTAC Kinetics Committee recommendations for performing kinetic computations on thermal analysis data. *Thermochim. Acta* **2011**, *520*, 1−19.
(62) Meng, Z.; Yang, D.; Yan, Y. Study of carbon black oxidation behavior under different heating rates. *J. Therm. Anal. Calorim.* **2014**, *118*, 551−559.
(63) Song, J.; Alam, M.; Boehman, A. L.; Kim, U. Examination of the oxidation behavior of biodiesel soot. *Combust. Flame* **2006**, *146*, 589−604.

https://dx.doi.org/10.1021/acs.energyfuels.0c02063
Energy Fuels 2020, 34, 12960−12971